




Review

Non-Linear Analysis of Flat Slabs Prestressed with Unbonded Tendons Submitted to Punching Shear

Heraldo Brigo ¹, Luana J. Ashihara ¹, Marília G. Marques ² and Elyson A. P. Liberati ^{1,*}

¹ Civil Engineering Department, State University of Maringá, Maringá 87020-900, Brazil

² Institute of Exact and Technological Sciences, Federal University of Viçosa, Rio Paranaíba 38810-000, Brazil

* Correspondence: eapliberati@uem.br

Abstract: This article describes a numerical study for the evaluation of the punching shear behavior of non-adherent prestressed flat slabs without shear reinforcement. Nonlinear three-dimensional models were used, along with the finite element method (FEA) through the ATENA software in order to validate the constitutive models adopted for concrete and steel. The numerical results were compared with the experimental results. The results revealed a good agreement among load capacity, deformations, and cracking panorama, as well as the relation between numerical and experimental failure loads. After validation, a parametric study was carried out to analyze the influence of tendon spacing, slab thickness, and column rectangularity in prestressed flat slabs. Finally, the results obtained in the numerical models in relation to the failure load were compared with the estimated values for the failure load according to the main normative predictions dealing with the flat slab system.

Keywords: punching shear; flat slabs; prestressed concrete; non-linear analysis



Citation: Brigo, H.; Ashihara, L.J.; Marques, M.G.; Liberati, E.A.P. Non-Linear Analysis of Flat Slabs Prestressed with Unbonded Tendons Submitted to Punching Shear. *Buildings* **2023**, *13*, 923. <https://doi.org/10.3390/buildings13040923>

Academic Editor: Abdelhafid Khelidj

Received: 8 March 2023

Revised: 23 March 2023

Accepted: 28 March 2023

Published: 31 March 2023



Copyright: © 2023 by the authors. Licensee MDPI, Basel, Switzerland. This article is an open access article distributed under the terms and conditions of the Creative Commons Attribution (CC BY) license (<https://creativecommons.org/licenses/by/4.0/>).

1. Introduction

The flat slab system is characterized by slabs resting rigidly and directly on the columns. This system has become a very widespread constructive alternative due to the speed of execution and the reduction in the right foot, in addition to being able to provide more economical foundations and more flexible layouts.

The direct contact of the column with the slab provides high shear stresses and causes the punching phenomenon, which is basically the perforation of a plate caused by concentrated forces or forces that act in small areas [1], is characterized by a fragile break in the connection between the column and the slab, and may occur in different positions along the structure according to the loading and boundary conditions [2,3], as shown in Figure 1.

To improve the punching resistance without changing the thickness of the slab, alternatives, such as the use of shear reinforcement, an increase in the rate of longitudinal bars, or prestressed concrete, can be used. Studies have revealed the beneficial effects of applying prestressing with different characteristics, either with the use of inclined tendon layouts in flat slabs [1–7], or with the use of straight tendons without eccentricity [8], or even with the application of external forces in isolated slab models [9,10].

According to [3,10], the eccentricity of reinforcements usually produces bending moments opposite to those of external actions. This leads to smaller crack openings in the failure region and therefore increases the concrete's ability to transfer shear forces. The vertical components of the prestressing forces from inclined cables intercepted by the punching failure surface are in equilibrium with the deflection forces that can be transferred directly to the supported area. This component can thus be subtracted from the shear load transferred by the concrete, according to [10].

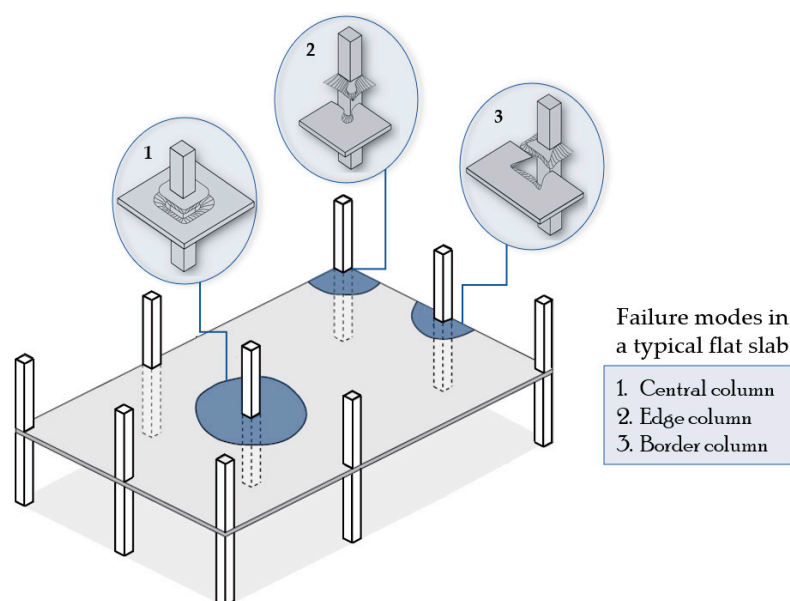


Figure 1. Punching phenomenon in reinforced concrete structures.

In view of the need to elaborate detailed projects, in recent decades, technology for dimensioning structures has advanced significantly. Increasingly, with the development of computers and software, numerical analyses of finite elements reach results close to those of experimental research. This type of analysis is very useful, particularly for the study of punching shear, given that carrying out experimental tests on slabs is often linked to high cost, in addition to the difficulty involved in its execution, especially in the case of prestressed slabs.

Although there is an increase in research focused on the use of finite element methods in flat slabs, more studies are needed involving the effect of punching in slabs and the use of prestressed concrete. In addition, more expressive normative instructions present different approaches and criteria for the design and detailing of the prestressing, as well as for the relationship between the tensile strength in the tendons and the shear strength in the slab–column contact. Hence, it is important to evaluate the criteria and recommendations established in normative codes such as [11–14].

Therefore, the objective of this work is to study the behavior of prestressed flat slabs with non-adherent tendons subjected to punching shear through non-linear numerical analyses, and furthermore to evaluate from calibrated models the spacing of the prestressing tendons, the thickness of the slab, and the rectangularity of the column. The values of failure loads, displacements, strains, and crack propagation were also compared. This comparison among results of numerical and normative analyses is necessary, as each of these recommendations presents different parameters for verifying the phenomenon of punching with prestressing.

2. Numerical Analysis

Due to the high cost of carrying out experiments, finite element analysis (FEA) has been used by researchers to study the interference of prestressing in slabs subjected to punching. When properly calibrated, the non-linear analysis by FEA can be used to study parameters that are difficult to measure experimentally and have not yet been investigated.

The investigation of the punching effect on flat slabs through numerical models is not recent. However, it is observed that both experimental and numerical studies involving the use of prestressing in this structural stem system are limited. Though incipient, ref. [15–17] stand out, as the authors were able to contribute to a better understanding of the punching phenomenon in prestressed flat slabs.

Considering the use of several pieces of commercial software for numerical analysis, the investigations of this work will be through calibration and performance of a parametric study based on the constitutive model implemented in the ATENA 3D software [18], which combines the traction behavior (fracture) and compression (plastic). The fracture model is based on the classic orthotropic smeared crack formulation and on Bazant's crack band model [18,19]. In this context, the Rankine rupture criterion is used, namely exponential smoothing, which was used in the fixed crack model. The plastic hardening or softening model is based on the Menétrey–William rupture surface [18,20].

This model uses algorithm return mapping, which is used for the integration of the constitutive equations, described in [21]. The model proposed by [22], which is based on a recursive substitution which allows two criteria, tension, and compression, to be improved and formulated separately. It can withstand cases in which the failure surface of both models has been reached, as well as when physical changes, such as crack closure for instance, occur. This model can be used to simulate concrete cracking, crushing due to confinement, and physical changes such as crack closure because of concrete crushing in another direction [18].

2.1. Solution Methods

For numerical analyses, it was decided to model only one-quarter of the slab, taking advantage of the symmetry in both directions. For pre-processing, the program GiD version 15.0.3 was used. The concrete, the plates, and the column were simulated with 3D hexahedral elements of the brick type containing 8 to 20 nodes. The size of the elements was determined by structured division in the volume of the model, in order to seek the value to the closest 25 mm³.

For the longitudinal reinforcement, bar-type elements were assigned and perfectly set in the concrete, with two nodes. The concept of discrete reinforcement was used, in which the bars are inserted, one by one, with determined spaces. The prestressing was applied by elements of the external tendon type, by the *CExternalTendon* command, without connection or crimping with the concrete, except for the extremity points where the prestressing force and the anchors are applied.

To determine the models, the Newton–Raphson interactive method was used, with the line search technique activated. The interaction limit was maintained at the default value adopted by the software of 30. The tolerance criteria used were 10^{−2}, 10^{−2}, and 10^{−4}, for displacement, force, and residual energy, respectively.

2.2. Concrete

The behavior of the concrete implemented in ATENA 3D was considered using the distributed fixed crack model approach, which is based on the modified compression field theory formulations proposed by [23]. The behavior of concrete is assumed for compression and tension, as shown in Figure 2.

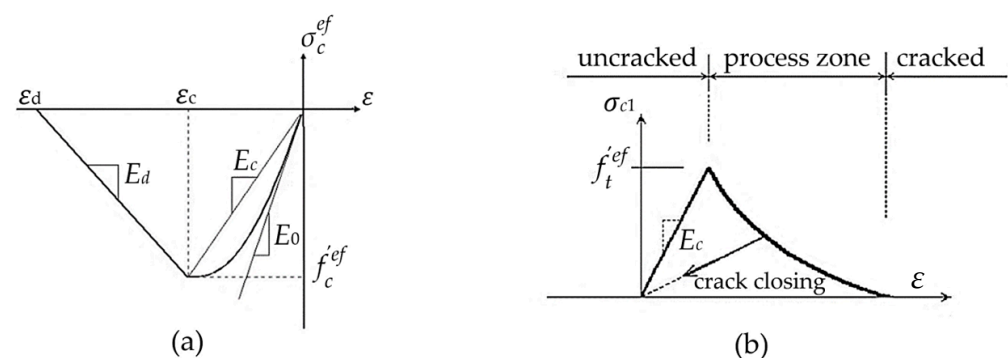


Figure 2. (a) Compressive stress–strain diagram; (b) stages of crack opening [18].

In compression (Figure 2a), prior to concrete crushing, the formulation by [24] is used, as a parabolic function, adopted for the ascending branch of the stress–strain function, and the damage is assumed as a non-linear response. After concrete crushing, the softening law is linearized. The dummy plane of compression model assumes that crushing because the compression is located in a plane normal to the direction of the principal compressive stress [18].

In tension (Figure 2b), this model considers a linear elastic stress–strain relationship, and a reduction in the compressive strength of concrete after cracking in the direction parallel to the cracks, which occurs when the effective tensile stress f_t^{lef} is reached. This crack opening function was experimentally derived by [25], according to Equation (1).

$$\frac{\sigma}{f_t^{lef}} = \left\{ 1 + \left(\frac{w}{w_c} \right)^3 \right\} \exp \left(-c_2 \frac{w}{w_c} \right) - \frac{w}{w_c} (1 + c_1^3) \exp(-c_2) \quad (1)$$

$$w_c = 5.14 \frac{G_f}{f_t^{lef}}$$

in which w is the crack width, w_c is the crack width where the stress is zero, and σ is the normal stress in the crack. The constant values are $c_1 = 3$ and $c_2 = 6.93$. The parameter G_f represents the fracture energy required for the crack to be stress-free. The standard value adopted by the program was based on [26], as shown in Equation (2).

$$G_f = 0.000025 f_t^{lef} \quad [\text{MN/m}] \quad (2)$$

Concrete failure is adopted following the work of [18,27]. In compression, it is represented by Figure 3, and can occur in two ways, either by biaxial stress, Equation (3), or by a state of tensile stress with compression, Equation (4). The failure function continues linearly from the point $\sigma_{c1} = 0$ and $\sigma_{c2} = f'_c$ to the region of tension with compression, with a linear decrease in force.

$$f_c^{lef} = \frac{1 + 3.65a}{(1 + a)^2} f'_c \quad \text{where : } a = \frac{\sigma_{c1}}{\sigma_{c2}} \quad (3)$$

$$f_c^{lef} = f'_c r_{ec} \quad \text{which is : } r_{ec} = \left(1 + 5.3278 \frac{\sigma_{c1}}{f'_c} \right), \quad 1.0 \geq r_{ec} \geq 0.9 \quad (4)$$

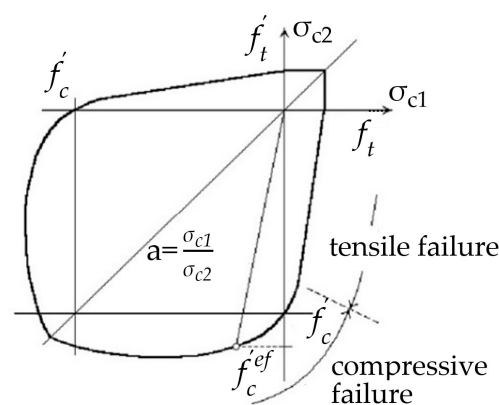


Figure 3. Biaxial failure function for concrete [18].

Tensile failure occurs in the state of tensile stress with tension, which is when the tensile force is constant and equal to the uniaxial tensile force f'_t . In the state of tensile stress with compression, the tensile force is reduced by Equation (5).

$$f_t^{lef} = f'_t r_{et} \quad \text{where : } r_{et} = 1 - 0.95 \frac{\sigma_{c2}}{f'_c} \quad (5)$$

where σ_{c1} and σ_{c2} are the principal stresses in concrete, f'_c is the uniaxial cylinder strength, r_{ec} is the reduction factor of the compressive strength in principal direction two due to the tensile stress in principal direction one, and r_{et} is the reduction factor of the tensile strength in principal direction two due to the compressive stress in principal direction one.

For the models in reinforced concrete, the effect of tension stiffening was attributed to them, which considers a contribution of the cracked concrete to the stiffness in relation to the traction of the steel bars. The tensile stress cannot fall below the value given by the product of $C_{ts}f_t$ (Figure 4). The recommended default value for $C_{ts} = 0.4$ was considered, as indicated by the model code [14].

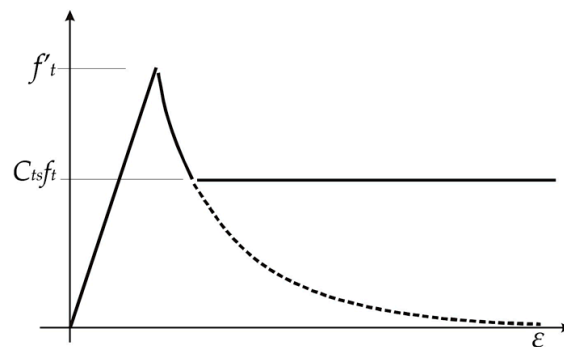


Figure 4. Tension Stiffening [18].

2.3. Steel

The perfect elastic-plastic bilinear law is assumed for the steel plates and the column. For the longitudinal reinforcement, the material was modeled considering a bilinear stress–strain relationship with a hardening model. Furthermore, perfect adhesion was assumed for the connection between the bending reinforcements with the surrounding concrete, based on [18,28]. The prestressing tendons were also considered in the bilinear relationship, by assigning the value 0 for friction and cohesion.

3. Numerical Models

In the experimental program carried out by [1], six flat slabs were tested, of which three were of reinforced concrete and the remaining three of prestressed concrete with unbonded tendons. All slabs had dimensions of $250 \times 250 \text{ cm}^2$ and a thickness of 160 mm. This experimental program used to calibrate the numerical models. In this section, the modeling of slabs M1 (reinforced concrete) and M4 (prestressed concrete) will be presented. Both models were without shear reinforcement.

The M1 and M4 slabs were supported by a thick steel plate $180 \text{ mm} \times 180 \text{ mm} \times 120 \text{ mm}$ on their central plan. Upward loading was applied incrementally by a hydraulic jack below the plate and was measured by a load cell located between the jack and plate. The centered reaction was transferred to the slab by a set of metal beams held in a reaction slab (Figure 5a).

In the first stage of the numerical modeling, a study was carried out with the specific objective of determining the type of element and the discretization that best represent the results in an adequate time. Two types of elements were used, hexahedral and tetrahedral, and the number of divisions in the thickness of the slab, whether into two, four or six parts, was varied. After analyzing the results, the type of hexahedral element with six divisions in the thickness of the slab was adopted, as it presents the lowest displacement error, in addition to good convergence for the failure load.

3.1. M1 Slab in Reinforced Concrete

The superior passive reinforcement was composed of a mesh of 16 mm bars every 100 mm (flexural reinforced ratio, $\rho = 1.58\%$), employed at an effective depth of 16.6 mm. In the bottom reinforcement were used bars of 8 mm every 100 mm.

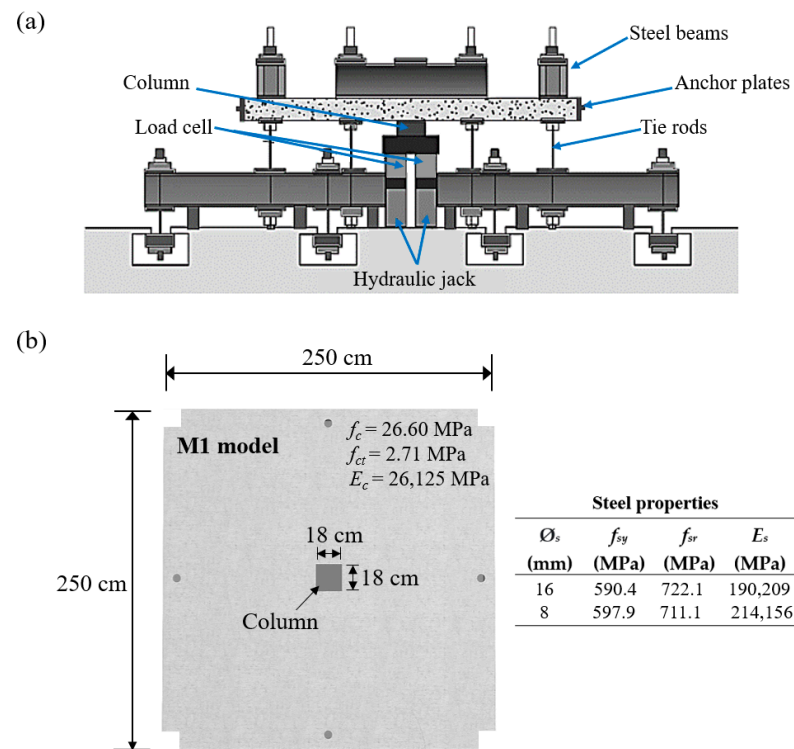


Figure 5. (a) Test setup, (b) M1 slab characteristics [1].

The concrete and reinforcement properties are described in Figure 5b, where f_c is the strength of concrete, f_{ct} is the tensile strength of concrete, E_c is the modulus of elasticity of concrete, \varnothing_s is the steel diameter, f_{sy} is the yield stress of steel, f_{sr} is the failure strength of steel, and E_s is the modulus of elasticity of steel.

To make the numerical model, the guidelines imposed by the experimental model are followed, as shown in Figure 6.

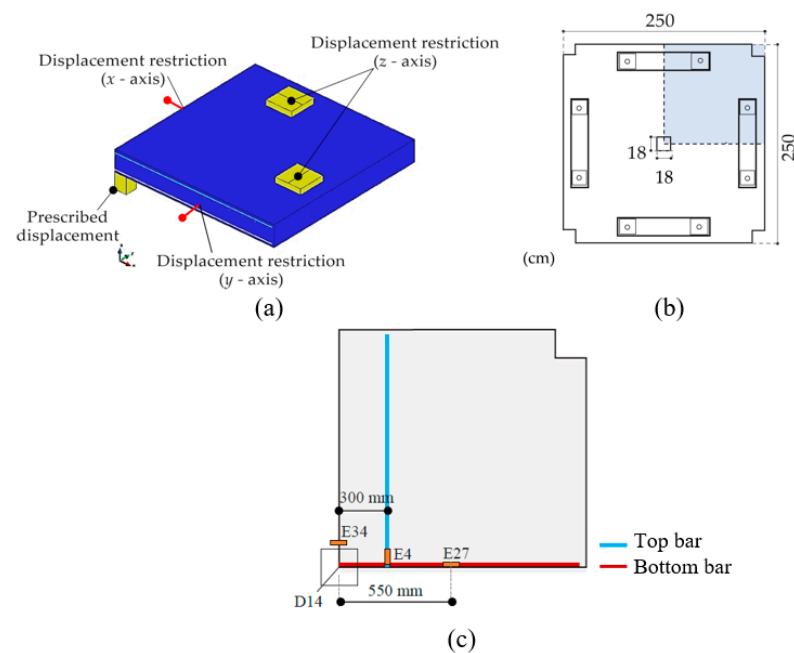


Figure 6. (a) Numerical model M1 and boundary conditions, (b) Characteristics of the experimental model, and (c) Position of extensometers on the reinforcement.

In the beginning, an incremental displacement of 0.1 mm was used on a steel plate that simulated the column in the center of the slab, with an *interval multiplier* of 100 times, divided into 200 steps, which established the total displacement of 10 mm. Restrictions were imposed to prevent horizontal displacements on the symmetry axes, in addition to vertical restrictions on the z-axis on the upper steel plates, to prevent vertical displacement.

The good convergence of the modeling results can also be confirmed through the load versus deformation curve (Figure 7c) at point E4, located in the upper tensile reinforcement, with extensometers positioned on the lateral faces of the bar. In the numerical model, the monitoring point was placed at the geometric center of the bar. In Figure 7d, the load versus strain curve for the bar compressed at position E27 is compared. It is possible to observe that in both monitoring points the numerical model was able to represent the trend of the curve of the experimental measurement point.

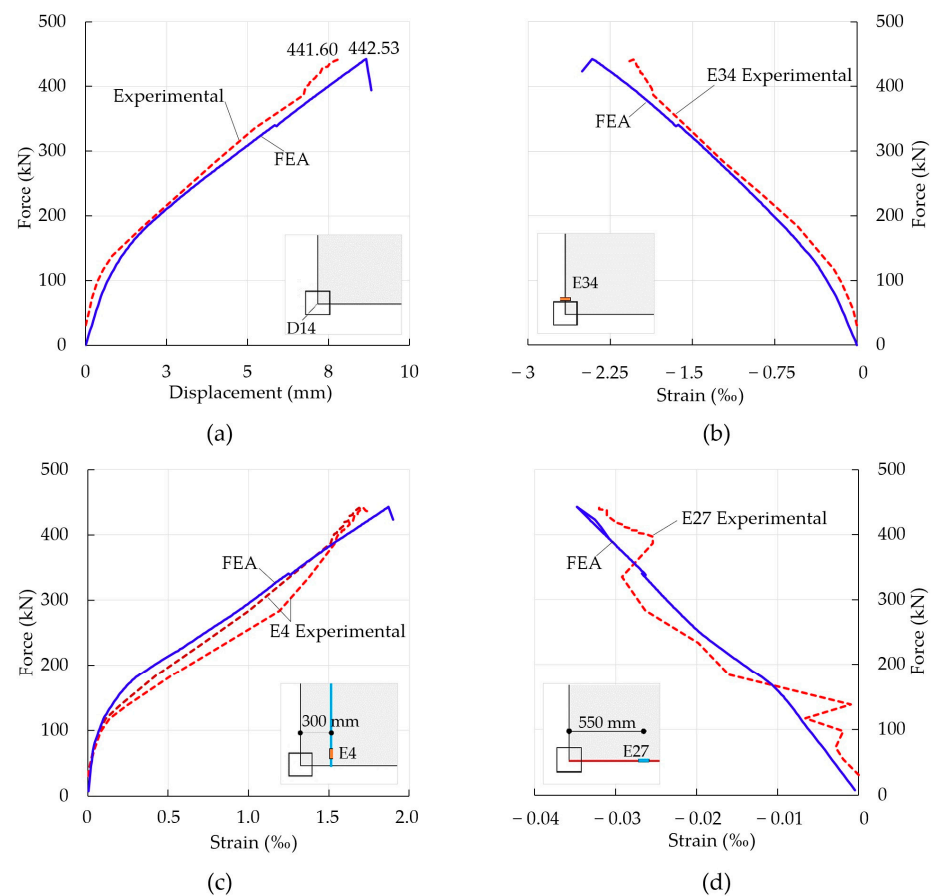


Figure 7. Comparison of numerical and experimental results of the M1 model.

Crack propagation can also be analyzed using volumetric strain, as shown in Figure 8. The first crack appears at a load of $0.25V$, and as expected for a structural model subjected to punching, in the center of the column and, with the increase in load, it continues towards the edge of the slab, in addition to the fact that the model is able to capture the tangential cracks in the surface. It is also notable that the radial cracks were influenced by the direction of the upper reinforcement bars. As observed in Figure 8b,c, the evolution of the cracks in the thickness of the slab coincides with the expected cracking of a punching failure. The initial appearance of cracks is caused by bending (straight lines) and the appearance of inclined cracks around the column is in the shear strength phase.

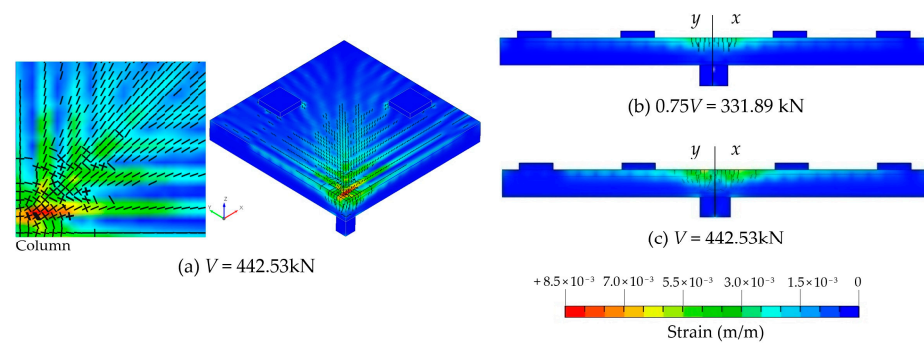


Figure 8. Cracking pattern on M1 model.

3.2. M4 Slab in Prestressed Concrete

The M4 slab respects the same characteristics of dimensions and loading scheme as the M1 slab. Its material properties are shown in Table 1. As a superior passive reinforcement, a mesh of 12.5 mm bars was used every 100 mm ($\rho = 0.92\%$ —flexural reinforced ratio) and at an average height of 12.8 mm. As an inferior passive reinforcement, a mesh with bars of 8 mm every 100 mm was adopted. As prestressing, 16 non-adherent tendons of type CP-190 RB 7 were used.

Table 1. Mechanical properties of materials, model M4 [1].

| Concrete Properties | | | Prestressing Tendon Properties | | | | Steel Properties | | | |
|---------------------|-------------------|----------------|--------------------------------|-----------------------------|--------------------|----------------|-------------------------|-------------------|-------------------|----------------|
| f_c (MPa) | f_{ct} (MPa) | E_c (MPa) | \varnothing_p (mm) | A_p (mm ²) | V_p (1%) (kN) | E_p (MPa) | \varnothing_s (mm) | f_{sy} (MPa) | f_{sr} (MPa) | E_s (MPa) |
| 51.92 | 3.87 | 30.46 | 12.7 | 99.9 | 182 | 208,000 | 12.5 | 651.4 | 792.3 | 201,541 |
| | | | | | | | 8.0 | 601.8 | 711.9 | 206,900 |

Note: f_c is the compressive strength of concrete, f_{ct} is the tensile strength of concrete, \varnothing_p is the equivalent diameter of a prestressing tendons, A_p is the tendon's area, V_p is the vertical component of tendon force acting on a specified section, E_p is the modulus of elasticity of tendons.

In Figure 9a, the numerical model that will be used for this analysis is presented and in Figure 9b are the geometric characteristics referring to prestressing. In the discretization, the anchor plates of the tendons were included. The forces recorded on the strands are in accordance with Table 2.

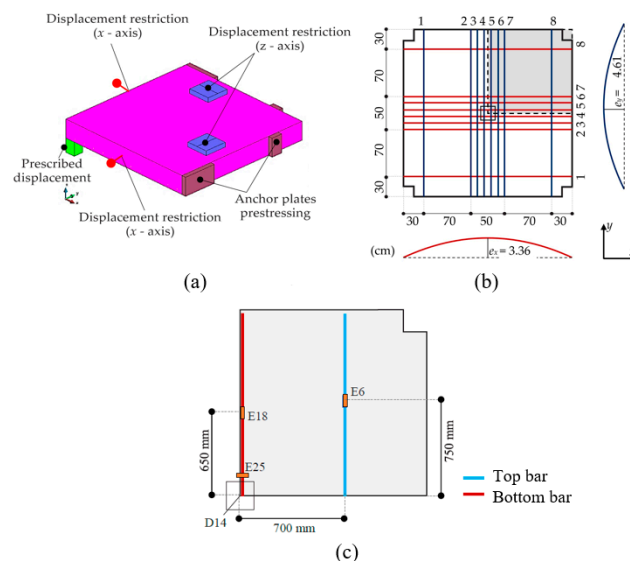


Figure 9. (a) Numerical model M4 and boundary conditions, (b) Characteristics of the experimental model, (c) Position of extensometers on the reinforcement.

Table 2. Prestressing force on tendons (kN) [1].

| Tendon | Direction x | | | | Direction y | | | |
|--------------|---------------|--------|--------|--------|---------------|--------|--------|--------|
| | 5 | 6 | 7 | 8 | 5 | 6 | 7 | 8 |
| Prestressing | 97.09 | 94.38 | 121.10 | 95.24 | 93.53 | 97.59 | 85.80 | 98.24 |
| Re-stress | 128.77 | 129.61 | 133.21 | 130.61 | 128.65 | 132.29 | 127.48 | 131.94 |
| Rupture | 136.03 | 137.89 | 140.07 | 134.10 | 137.15 | 141.03 | 134.88 | 135.52 |

Numerical analysis will follow the same steps described in the experimental process. To represent the test procedure with the greatest fidelity as possible, the numerical model was divided into three loading intervals, namely:

1. Application of incremental displacement on the column until the slab reaches a reaction of 80 kN.
2. Application of a standard force on each of the prestressing tendons by the command *Prestressing for reinf line*, under boundary conditions.
3. At the end of prestressing, the master-slave node connections between the end of the tendon and the node closest to the anchor plate are activated. Finally, incremental displacement is applied to the column until the slab reaches failure.

The modeling started from the final parameters established for slab M1. At first, the results revealed that, for a better convergence, the force applied to the tendons must be considered with the experimental values of re-stressing (Table 2) and the tension stiffening effect must be neglected in models with pre-stressing.

Given these observations, the comparison of the results with the experimental model was undertaken by taking the load–displacement curve at the center of the slab (D14). The curves in Figure 10a show that in the prestressing application stage, the experimental curve presented oscillations, which were not observed in the numerical model and are justified by the fact that prestressing was applied simultaneously to all tendons, with complete restriction of vertical displacement in the column. At the end of prestressing, the numerical model reached 218.74 kN, a value very close to the 221.30 kN of the experimental model. After prestressing, it is observed that the numerical response was able to reproduce the trend in the final section of the test curve, reaching the final load and displacements of 785.06 kN and 8.79 mm. The V_{FEA}/V_{exp} ratio was 1.016, which is sufficiently accurate.

For concrete strain, it was placed on the underside of the slab in position E25, tangentially to the column. A good convergence of the numerical model is represented by the curve in Figure 10b, with the experimental result. There was a small discrepancy only in the initial phase when prestressing is applied. In Figure 10c, it is possible to observe how the curve obtained numerically for position E6, of a tensioned bar, was able to maintain itself between the two extensometers, which represents a good average of the predicted behavior. In the case of position E18, of a compressed bar, until the end of prestressing, the curve (Figure 10d) manages to capture the strains well; after prestressing, the curve of the numerical model was able to capture the trend of the experimental curve.

The cracking panorama is also shown in Figure 11. The first crack appears at 0.45V, proving that cracking control obtained in the concrete occurred in a controlled manner when compared to the M1 model, which can be explained by the application of prestressing.

The panorama of radial cracks evolved as in model M1 and followed the direction of the upper flexed bars to the edge of the model. Close to failure (Figure 11c), it is possible to identify inclined cracks in the thickness of the slab and tangential cracks around the column, which form a punching cone, as expected.

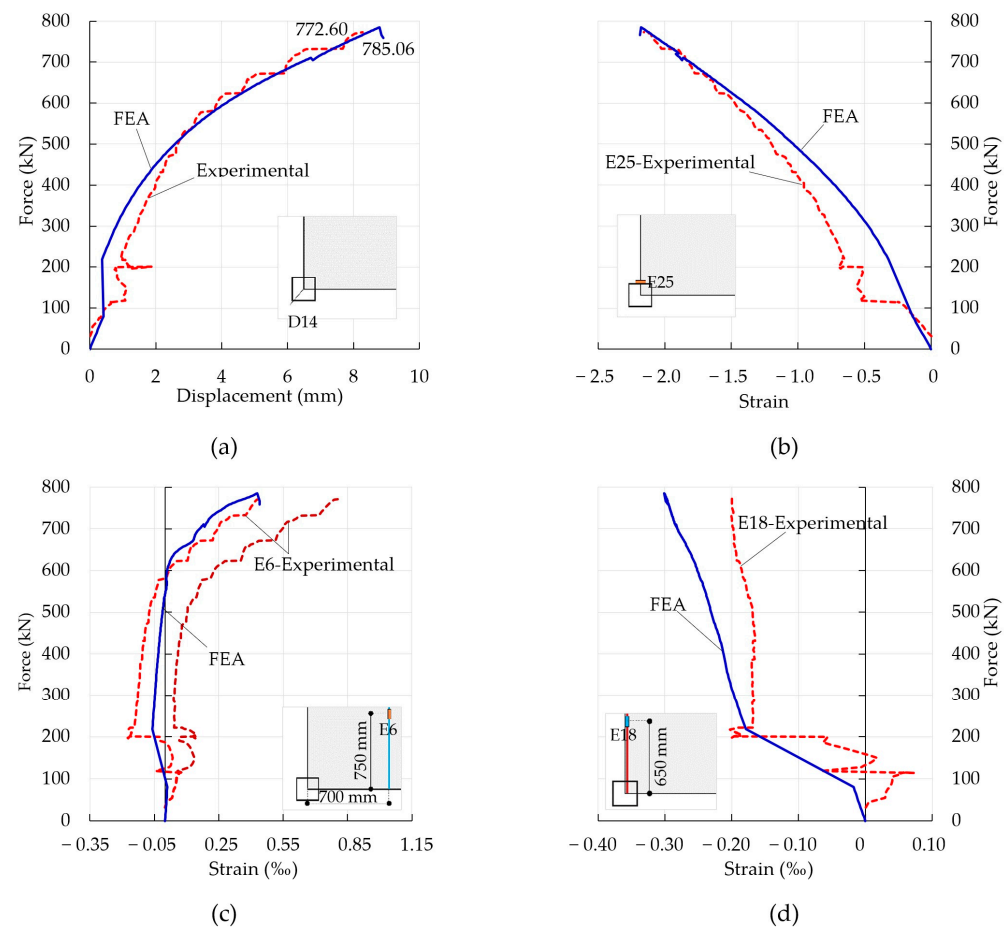


Figure 10. Comparison of numerical and experimental results of the M4 model.

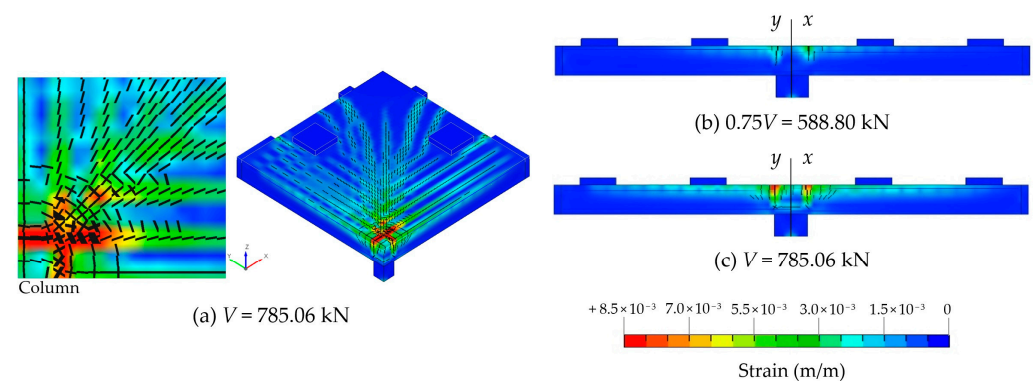


Figure 11. Cracking pattern on M4 model.

4. Parametric Study

A parametric study was carried out with the aim of evaluating the influence of pre-stressing on punching resistance. The characteristics of the new models are maintained according to the M4 model of the previous section, so that items such as geometry, materials, longitudinal reinforcement rate, and the characteristics of the prestressing tendons and the force applied to them, as well as boundary conditions and monitoring points, will be preserved. For each variable studied, all the characteristics of the model were maintained, with changes only in the analyzed parameter.

Therefore, 25 new models were evaluated along with the M4 reference model, which were divided into three series with the following variables:

- Series A: three models varying the spacing between the central prestressing tendons;

- Series T: seven models varying the thickness of the slab;
- Series C: fifteen models varying the column rectangularity.

The three new models of Series A (Figure 12), correspond to the spacing between the prestressing tendons in the central region of the slab (5 cm, 10 cm, 15 cm, and 20 cm). These are defined in the nomenclature by the term ‘series spacing’. In this way, the model from Series A with spacing of 5 cm is represented as A-5.

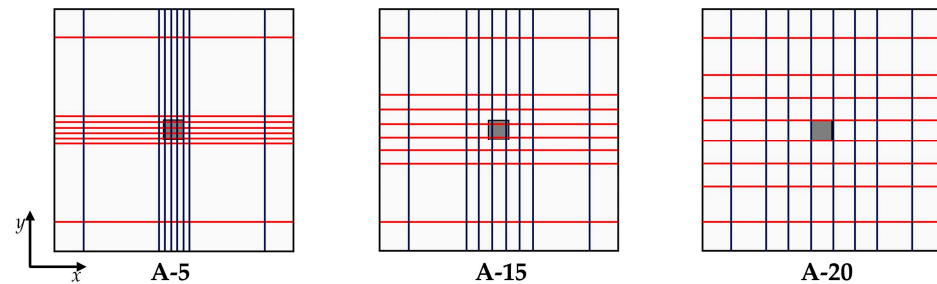


Figure 12. Plan view of the Series A prestressing tendons.

For Series T, the seven new models analyzed refer to the thickness of the slab, and their nomenclature is ‘series thickness’. In this way, the Series T model with a thickness of 18 cm is represented as T-18. The reference model corresponds to the 16-cm thick M4 model (T-16). The eccentricity of the prestressing tendons was kept unchanged, as shown in the four examples in Figure 13. The hexahedral mesh was maintained, and the models were adjusted to ensure elements with dimensions closer to 25 mm³.

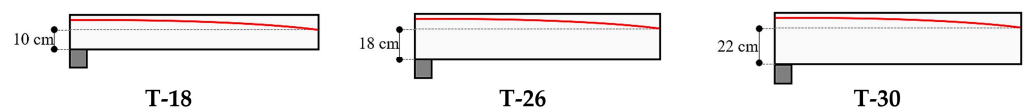


Figure 13. Thickness settings on Series T models.

The 15 new Series C models refer to the rectangularity of the slab’s support column. The variations started from an 18 × 20 cm column, with an addition of 5 cm in the direction of the x axis, as shown in Figure 14, without exceeding five times its smallest section and being limited to 90 cm, which gave rise to the 15 new models.

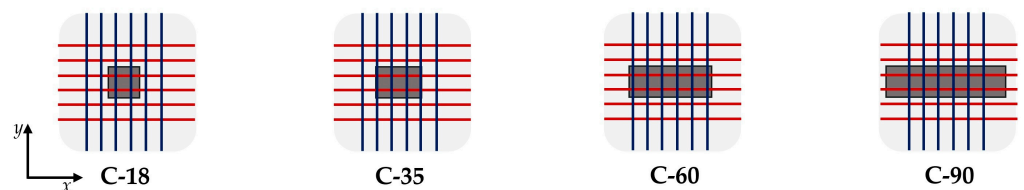


Figure 14. Column dimension settings on Series C models.

The nomenclature created to facilitate the understanding of these segments is ‘column size series’. In this sense, the 20 cm Series C column appears as C-20. The M4 model refers to the reference slab C-18.

Comparison of Results

This item presents the results of the three analyzed series. The monitoring points were maintained according to the M4 model, thus making it possible to compare the new results obtained with those already presented for the numerical model. The ultimate loads (V), displacement and maximum strain in concrete ($\epsilon_{c,m\acute{a}x}$), and the V/V_{M4} ratio were analyzed.

In Table 3, the respective maximum values of each slab of Series A are compared. It is noticeable in this scenario that, when increasing the spacing between the tendons, there is a reduction in punching resistance. It is also observed that the A-5 model, with

smaller spacing, presented a slight increase in resistance, which is also justified due to the contact area of the slab surface with the column coinciding with two prestressing tendons (Figure 12).

Table 3. Results obtained with Series A.

| Models | V (kN) | $\frac{V}{V_{M4}}$ | Displacement (mm) | $\varepsilon_{c,m\acute{a}x}$ (‰) |
|--------|-----------|--------------------|----------------------|--------------------------------------|
| A-5 | 788.12 | 1.00 | 8.89 | −2.08 |
| A-10 | 785.06 | 1.00 | 8.79 | −2.18 |
| A-15 | 753.17 | 0.96 | 7.85 | −2.04 |
| A-20 | 690.83 | 0.88 | 6.31 | −1.77 |

Note: V_{M4} is the failure load of slab M4 obtained experimentally by [1].

Regarding concrete strain, in all four models a similarity between their behaviors is observed. In addition to a greater gain in resistance, the reduction in the spacing between the tendons, in the A-5 model, helped to reduce the concrete strain ($\varepsilon_{c,m\acute{a}x}$). For the models with greater spacing, as shown in the table, a reduction in the maximum strain is observed, which indicates a more fragile rupture, justified by the anticipation of the rupture of models.

The crack patterns can be seen in Figure 15, where it was found that all analyzed models were consistent with the evolution of cracks observed in the numerical calibration model, M4 (equivalent to A-10), as presented in the test by [1].

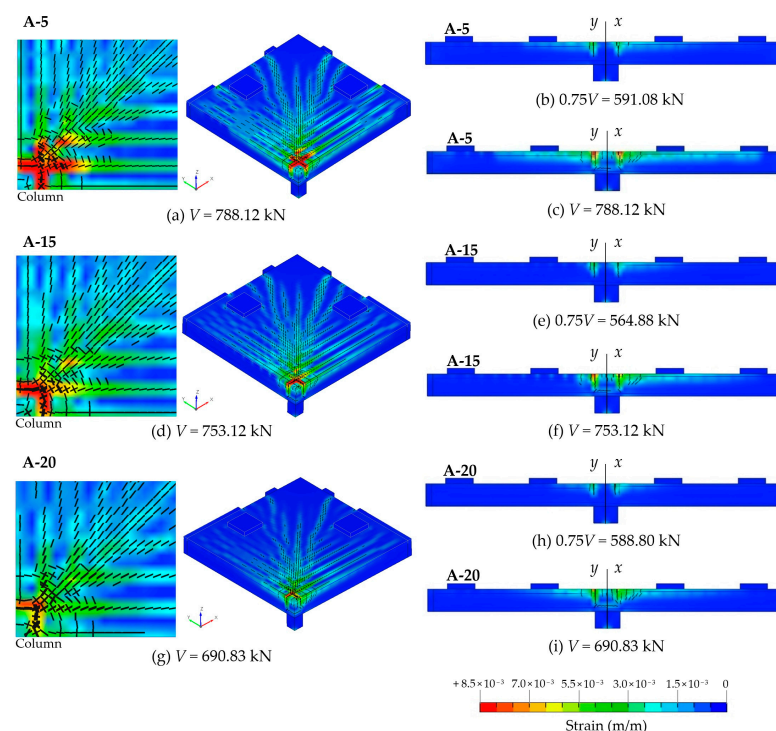


Figure 15. Cracking pattern of Series A models.

In general, the panorama of the radial cracks of the models followed the direction from the superior flexed bars of greater height to the margin. When it is close to failure, it is possible to identify how slab A-5 is able to withstand greater strains in relation to the others. The model also stands out as the one with the highest formation and distribution of cracks on the surface of the slab, which is justified by the fact that the prestressing stresses are concentrated in the region closest to the column, which makes the slab resist greater strains. In Figure 15a,d,g, it is also possible to identify a similarity of the tangential cracks regarding the thickness and surface of the slab (Figure 15c,f,i) around the column, something characteristic of the punching cone formation. As the figures are presented, the

spacing of the tendons interferes not only with the capacity of the slab, but also with the concentration of cracks.

Following the study, the load (V), displacement, and maximum strain in concrete ($\varepsilon_{c,max}$) and the V/V_{M4} ratio of the Series T are compared and are presented in Table 4. Based on the presented data, it is noticeable how alterations in the thickness of the slab interfere in its capacity of resistance and in the rigidity of the models. The configurations showed contributions from 16% to 138% for the ultimate load and, for some, a displacement reduction of up to 20%. Regarding the strain of the concrete, a behavior very similar to that of the reference slab E-16 is observed, with a reduction of -5.77% for the E-30 model.

Table 4. Results obtained with Series T.

| Models | V (kN) | $\frac{V}{V_{M4}}$ | Displacement (mm) | $\varepsilon_{c,max}$ (‰) |
|--------|-------------|--------------------|----------------------|------------------------------|
| T-16 | 785.06 | 1.00 | 8.79 | −2.08 |
| T-18 | 909.46 | 1.16 | 7.04 | −2.04 |
| T-20 | 1059.23 | 1.35 | 6.22 | −2.00 |
| T-22 | 1187.16 | 1.51 | 5.33 | −1.90 |
| T-24 | 1408.22 | 1.79 | 5.62 | −2.04 |
| T-26 | 1534.49 | 1.95 | 4.81 | −1.95 |
| T-28 | 1669.18 | 2.13 | 4.19 | −1.86 |
| T-30 | 1870.16 | 2.38 | 4.22 | −1.96 |

With the tabulated results, it is evident that the increase in the amount of concrete contributed to the increase in the capacity and stiffness of the slabs. In addition, the gain in resistance was mainly due to the additional amount of concrete.

The cracking landscape was compared among the T-18, T-22, and T-30 models. As seen in Figure 16, the cracks evolved as expected for models subjected to punching, starting radially, and then following the direction of the upper bars to the margin.

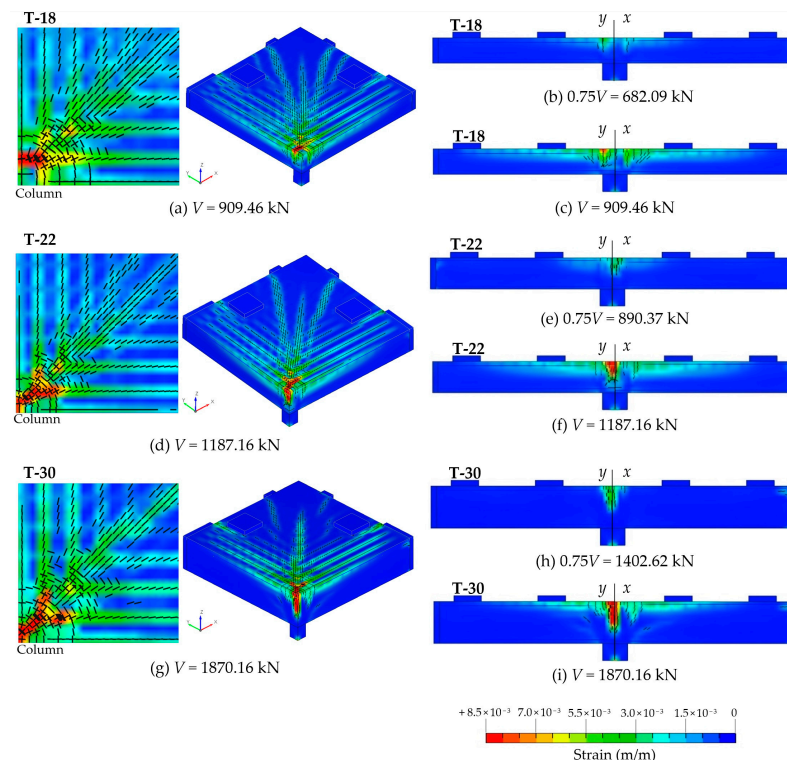


Figure 16. Cracking pattern of Series T models.

When it is close to failure, it is possible to identify how the T-30 slab (Figure 16g) concentrates greater shearing efforts in a more central and superior point, while the thinner models start this process in the contour of the face of the column. This means that, in thicker slabs, there is a concentration of greater strains before failure in a more central point and on the upper surface.

In Table 5, the results of Series C are presented, which investigated the impact of column rectangularity on the capacity to resist punching of prestressed flat slabs, where the maximum values of load (V), displacement, and strain in concrete ($\epsilon_{c,max}$) and the V_C/V_{M4} ratio of the 16 slabs were analyzed.

Table 5. Results obtained with Series C.

| Models | V (kN) | $\frac{V}{V_{M4}}$ | Displacement (mm) | $\epsilon_{c,max}$ (‰) |
|--------|-----------|--------------------|----------------------|---------------------------|
| C-18 | 785.06 | 1.00 | 8.79 | −2.08 |
| C-20 | 812.31 | 1.04 | 9.54 | −2.28 |
| C-25 | 846.78 | 1.08 | 10.02 | −1.93 |
| C-30 | 847.04 | 1.08 | 9.61 | −1.55 |
| C-35 | 833.47 | 1.06 | 8.51 | −1.10 |
| C-40 | 869.48 | 1.11 | 9.09 | −0.98 |
| C-45 | 932.41 | 1.19 | 10.26 | −0.85 |
| C-50 | 977.14 | 1.24 | 10.89 | −0.76 |
| C-55 | 917.22 | 1.17 | 8.65 | −0.46 |
| C-60 | 1019.94 | 1.30 | 11.16 | −0.50 |
| C-65 | 1047.08 | 1.33 | 10.85 | −0.25 |
| C-70 | 1064.57 | 1.36 | 10.63 | −0.16 |
| C-75 | 1014.59 | 1.30 | 9.19 | −0.02 |
| C-80 | 1047.25 | 1.33 | 9.87 | 0.11 |
| C-85 | 1129.02 | 1.44 | 10.59 | 0.27 |
| C-90 | 1200.37 | 1.53 | 12.11 | 0.28 |

The results show a great influence on the resistance capacity of prestressed flat slabs when changing the dimensions of a central column in relation to its rectangularity. With the maximum values indicated in Table 5, the gains observed from the C-60 model, with the ratio between the maximum and minimum column length of 3.33, were 30% higher. For the C-90 model, the observed gains were 53% higher in terms of resistance, and 37% higher in terms of maximum displacement.

Regarding the strain of the concrete, a great interference was observed in the behavior of the slabs as the dimensions of the column increased. The greatest variations in strain were reached by the slabs with the smallest contact area between the upper face of the column and the slab. From slab C-80, a positive variation in the strain results was more evident, indicating a tensile strain in the central region of the slab where the monitoring point was located.

The cracking panorama was compared for three Series C slabs, in which the C-20, C-50, and C-90 models were observed. At first, in all models, the cracks started at the corner of the column, radially following the direction of the upper bars to the margin. Figure 17a,d,g show what happens, at failure, with the cracking patterns on the surface under tension. A similarity is observed in both directions in the perpendicular cracks of the slab with the square column, C-20 (Figure 17a). As the rectangularity of the column increases, the cracking patterns are no longer as uniform as observed in square sections. Furthermore, the diagonal cracks on the surface become concentrated in the shortest corner of the column. The highest values of tensile strain observed in Figure 17g indicate that punching failure occurs on the faces with smaller dimensions of the column.

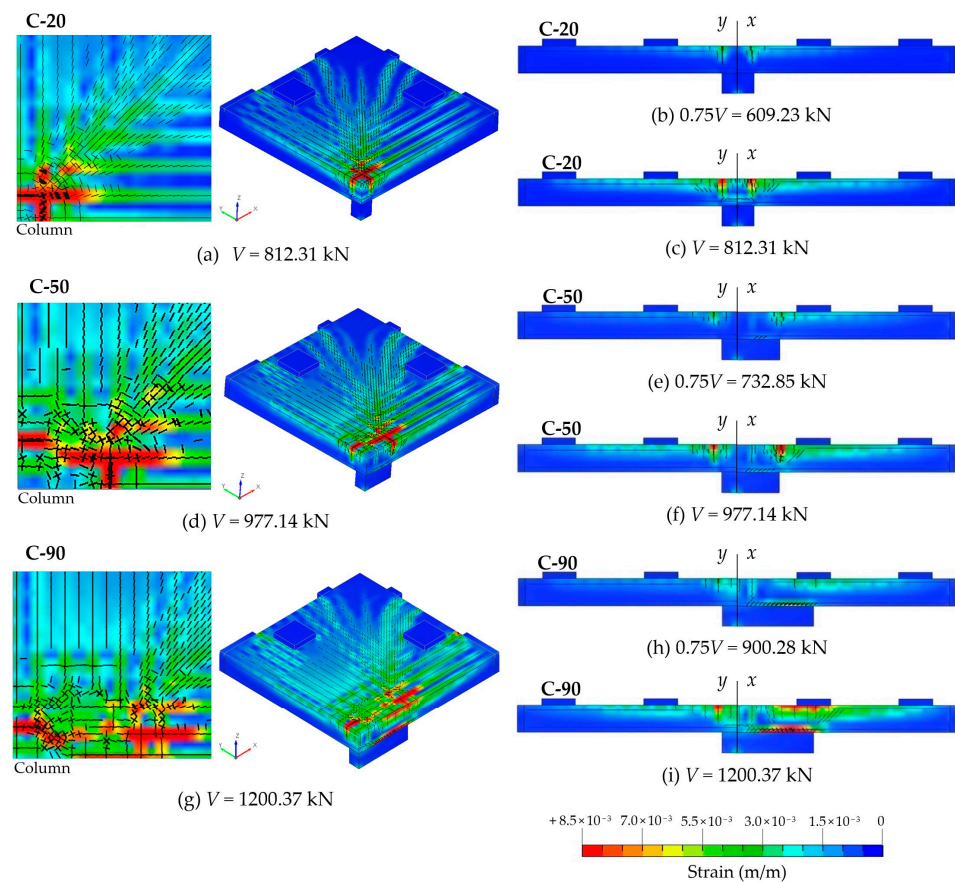


Figure 17. Cracking pattern of Series C models.

Another important point, in addition to the reduction in tangential cracks forming the punching cone, is the fact that the perpendicular cracks on the longer side of the column (Figure 17i) indicate a predominant behavior of directional shear on the longer side. It should also be considered that the increase in rectangularity causes a stress region on the lower surface of the slab, a movement not observed in square columns.

5. Normative Comparison

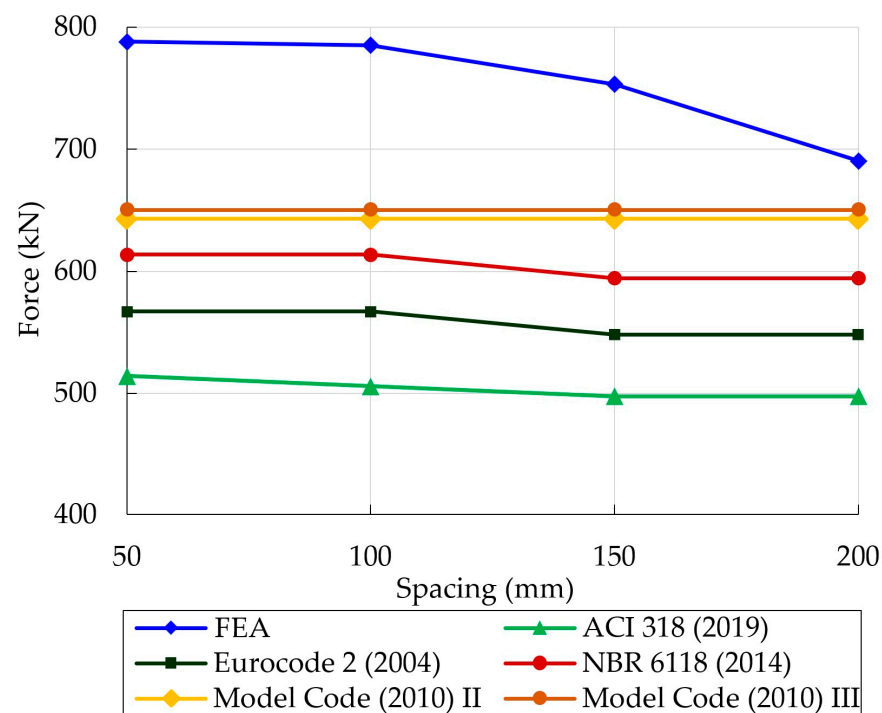
In this section, the numerical results of the three series of the previous section are compared with the punching resistance estimates predicted by ACI [11], Eurocode 2 [12], NBR [13] and Model Code [14], and LoA II and LoA III, using the equations in the Appendix A. For each series, the ultimate load ratio of the numerical models (V_{FEA}) is arranged with the estimated ultimate load predicted in the normative codes (V_R). For the calculation of the breaking load values, all partial safety factors provided for in the design codes were considered as equal to 1.

5.1. Comparison of Series A Results

Table 6 presents the results obtained numerically from the four models of Series A, and the V_{FEA}/V_R ratio, along with their respective mean values, standard deviation (SD.), and coefficient of variation (C.V.). Their respective breaking load evolution is shown in Figure 18.

Table 6. Comparison between numerical and theoretical breaking loads (Series A).

| Models | V_{FEA} (kN) | $\frac{V_{FEA}}{V_{R,ACI}}$ | $\frac{V_{FEA}}{V_{R,ECI}}$ | $\frac{V_{FEA}}{V_{R,NBR}}$ | $\frac{V_{FEA}}{V_{R,MC II}}$ | $\frac{V_{FEA}}{V_{R,MC III}}$ |
|----------|----------------|-----------------------------|-----------------------------|-----------------------------|-------------------------------|--------------------------------|
| A-5 | 788.12 | 1.53 | 1.39 | 1.28 | 1.23 | 1.21 |
| A-10 | 785.06 | 1.55 | 1.38 | 1.28 | 1.22 | 1.21 |
| A-15 | 753.17 | 1.51 | 1.37 | 1.27 | 1.17 | 1.16 |
| A-20 | 690.83 | 1.39 | 1.26 | 1.16 | 1.07 | 1.06 |
| Mea. | | 1.50 | 1.35 | 1.25 | 1.17 | 1.16 |
| SD. | | 0.06 | 0.05 | 0.05 | 0.06 | 0.06 |
| C.V. (%) | | 4.26 | 3.93 | 4.01 | 5.19 | 5.19 |

**Figure 18.** Failure load evolution in relation to the spacing of prestressing tendons (Series A) [11–14].

From the data presented, it is observed that the average results closest to the numerical values were obtained, respectively, by the equations of the *fib* model code [14] in its level III and II (LoA III and LoA II) of approximation, followed by the indices of the NBR [13] and EC2 [12]. Both numerical results had mean magnification indexes below 1.35, which is above those calculated using the equations. It is observed that the ACI [11] and EC2 [12] presented more conservative mean results, with indices corresponding to 50% and 35%, respectively, of those numerically obtained results.

It is important to observe that the results obtained by level III of the *fib* model code [14], despite better representing the numerical result, namely 1.17, were also those that obtained the highest variational coefficient, corresponding to 5.19%, which indicates a greater dispersion of results in relation to the average value. When evaluating the standard deviation indices and the average of the results obtained in Table 6, it is observed that both levels of approximation of the *fib* model code [14] were able to represent more uniform results, which are closer to the numerical models followed by the NBR [13].

Regarding the calculation model that each standard uses when considering prestressing in flat slabs, it can be noted, as shown in Figure 18, that the results estimated in ACI [11], EC2 [12], and NBR [13] for the A-15 Series were the same as those for the A-20 Series, while the *fib* model code [14] estimates were the same for all models. These results indicate that, in both design codes, only the prestressing force is considered, and the ultimate load of flat slabs is not estimated, considering the spacing between the tendons.

5.2. Comparison of Series T Results

The V_{FEA}/V_R ratio was also used to compare the normative codes and the numerical results obtained from the 8 Series T models, as shown in Figure 19.

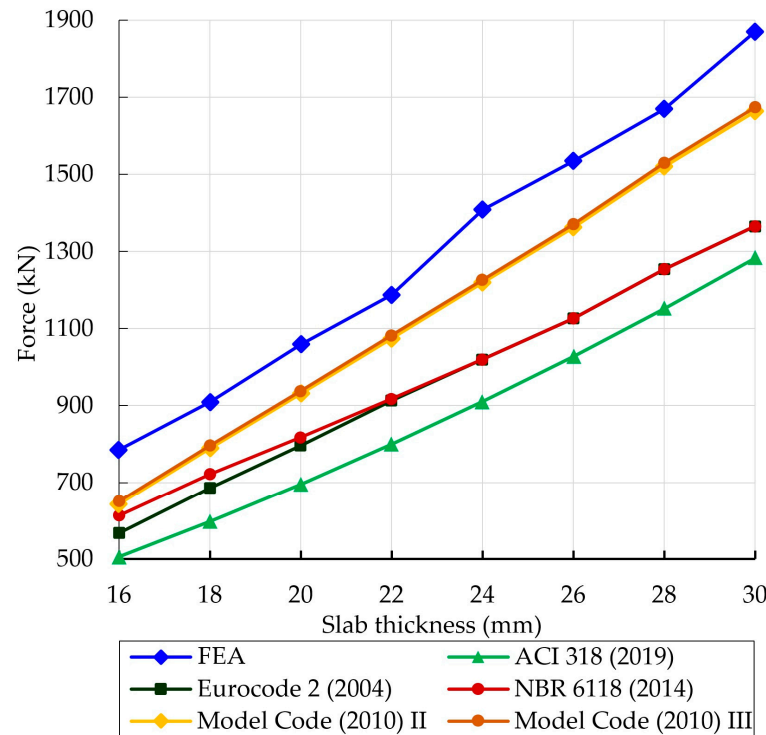


Figure 19. Failure load evolution in relation to the spacing of prestressing tendons (Series T) [11–14].

The results observed in Figure 19 indicate a tendency of evolution of the resistant capacity, which is foreseen in the normative codes for each analyzed model, as well as it is also observed in the numerical indices. It is noted that the ACI [11], EC2 [12] and NBR [13] tend to be more conservative in the results, with the best estimates presented by levels III and II of the *fib* model code [14], respectively. It is noticed that the best average results of the normative codes were obtained, respectively, by the equations of the *fib* model code [14], levels III and II, followed by the ACI [11], EC2 [12], and NBR [13], both with average results lower than 1.50 in relation to numerical models. The ACI [11] was the norm, with results farther from those predicted numerically, which always maintained an average ratio above 1.45.

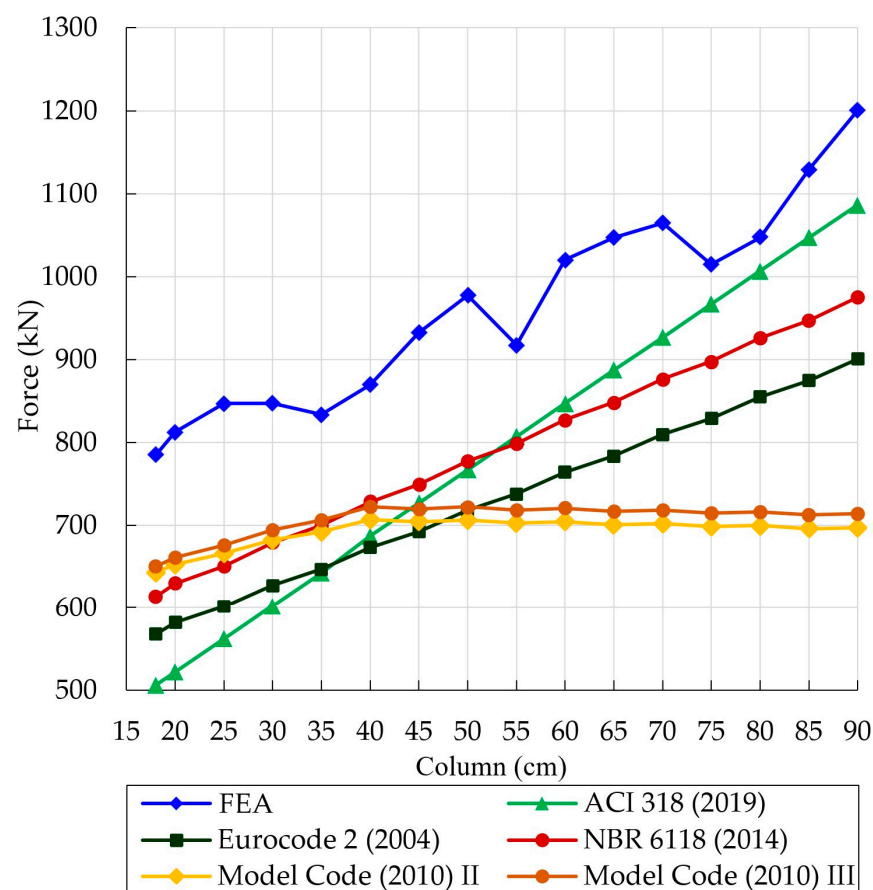
When each series was evaluated individually, there is a common tendency among the ACI [11] and *fib* model code [14] levels III and II to estimate results closer to numerically predicted as the thickness of the slabs becomes smaller. When comparing the results of Figure 19, it is noted that, from the T-24 Series, the EC2 [12] and the NBR [13] predict the same results, which is indicated because the standards share the same formulations, differing, however, in slabs of lesser thickness. These results are justified by the scale factor k , in which, up to the T-22 Series, EC2 [12] limits k as less than or equal to 2.0, while the Brazilian standard does not have this limitation. As an example, one can cite the slab T-16, in which the NBR [13] determines k equal to 2.22.

5.3. Comparison of Series C Results

The numerically obtained results of the 16 models of the Series C with their respective estimates of the breaking load from the normative instructions as provided by the V_{FEA}/V_R ratio are in Table 7, and the evolution of the failure estimate is shown in Figure 20.

Table 7. Comparison between numerical and theoretical breaking loads (Series C).

| Models | V_{FEA} (kN) | $\frac{V_{FEA}}{V_{R,ACI}}$ | $\frac{V_{FEA}}{V_{R,ECI}}$ | $\frac{V_{FEA}}{V_{R,NBR}}$ | $\frac{V_{FEA}}{V_{R,MC II}}$ | $\frac{V_{FEA}}{V_{R,MC III}}$ |
|----------|----------------|-----------------------------|-----------------------------|-----------------------------|-------------------------------|--------------------------------|
| C-18 | 785.06 | 1.55 | 1.38 | 1.28 | 1.22 | 1.21 |
| C-20 | 812.31 | 1.56 | 1.40 | 1.29 | 1.24 | 1.23 |
| C-25 | 846.78 | 1.51 | 1.41 | 1.30 | 1.27 | 1.25 |
| C-30 | 847.04 | 1.41 | 1.35 | 1.25 | 1.24 | 1.22 |
| C-35 | 833.47 | 1.30 | 1.29 | 1.19 | 1.20 | 1.18 |
| C-40 | 869.48 | 1.27 | 1.29 | 1.19 | 1.23 | 1.20 |
| C-45 | 932.41 | 1.28 | 1.35 | 1.24 | 1.32 | 1.30 |
| C-50 | 977.14 | 1.27 | 1.36 | 1.26 | 1.38 | 1.35 |
| C-55 | 917.22 | 1.14 | 1.24 | 1.15 | 1.31 | 1.28 |
| C-60 | 1019.94 | 1.20 | 1.34 | 1.23 | 1.45 | 1.42 |
| C-65 | 1047.08 | 1.18 | 1.34 | 1.23 | 1.49 | 1.46 |
| C-70 | 1064.57 | 1.15 | 1.32 | 1.21 | 1.52 | 1.48 |
| C-75 | 1014.59 | 1.05 | 1.22 | 1.13 | 1.45 | 1.42 |
| C-80 | 1047.25 | 1.04 | 1.22 | 1.13 | 1.50 | 1.46 |
| C-85 | 1129.02 | 1.08 | 1.29 | 1.19 | 1.62 | 1.58 |
| C-90 | 1200.37 | 1.11 | 1.33 | 1.23 | 1.72 | 1.68 |
| Mea. | | 1.26 | 1.32 | 1.22 | 1.39 | 1.36 |
| SD. | | 0.17 | 0.06 | 0.05 | 0.15 | 0.14 |
| C.V. (%) | | 13.26 | 4.17 | 4.18 | 10.94 | 10.66 |

**Figure 20.** Failure load evolution in relation to the spacing of prestressing tendons (Series C) [11–14].

As for the curves obtained by the *fib* model code [14], it is pointed out that for levels II and III, there is a stability of the results from Series C-40, which is justified due to the discontinuity of the critical perimeter b_1 , which, for the calculation check, considers that the maximum measurement of the column does not exceed $3d$. With this, it was observed

that 10 of the 16 models presented very conservative results, even at the highest level of the *fib* model code [14], which means that the equations require adjustments.

When evaluating Table 7, it can be seen that level II presented more conservative results in relation to the other norms, with an average of 1.39. However, it should be noted that the mean value and the variation in the results for the two levels of approximation was impaired due to the limited control perimeter in $3d$ (up to C-40). However, it should be noted that, up to the C-40 model, the *fib* model code [14] obtained the best approximations of results.

In Figure 20, it can be seen that the best results were due to the NBR [13], with a mean of 1.22 and a coefficient of variation of 4.17%. The highest $V_{R,FEM}/V_{R,NBR}$ ratio did not exceed 1.34, which indicates estimates always in favor of safety. Regarding Eurocode 2 [12], it can be noted that the results differ from the Brazilian standard due to the fact that its greater conservatism regarding the scale factor results in it being set at 2.0. The ACI [11] showed satisfactory results, with an average of 1.26; however, the dispersion percentage of 13.26% should be noted as well as the more satisfactory results in the models with columns of larger dimensions.

6. Conclusions and Suggestions for Future Investigations

The present work evaluated the behavior of prestressed concrete flat slabs under different design characteristics using non-linear numerical analyses, which were supported by ATENA software. The results reached through the numerical analyses were compared to those of the experimental models by [1], considering not only the comparisons of the curves of load versus displacement and load versus strain of concrete and longitudinal reinforcement, but also the cracking panorama, in which it was noticed that the models were able to correctly represent the behavior observed in prestressed flat slabs.

In view of the good convergence of results, it was possible to continue the research through a parametric study of new structural models. For this purpose, three series were determined, which were constituted considering the spacing between the prestressing tendons (Series A), the thickness of the slab (Series T) and the rectangularity of the column (Series C), where the following conclusions can be drawn:

1. Series A: the increase in spacing between tendons promoted a reduction in punching resistance and a decrease in concrete strain. The panorama of cracking of the slab with smaller spacing showed a greater concentration of cracks and strains, accompanied by an increase in resistance.
2. Series T: the thickness of the slab causes great interference in the resistance and rigidity capacity of the models. The models revealed that strains in thicker slabs tend to concentrate, before failure, in a more central point and on the upper face of the slab.
3. Series C: the rectangularity of the column has a great influence on the resistance capacity of prestressed flat slabs. Larger strains are achieved by slabs with a smaller column contact area. The larger support area for the prestressing tendons contributes to increased resistance.

When the estimates obtained with the normative codes were analyzed, it is concluded that:

1. Series A: in general, the rules worked in favor of safety. Note that the design codes did not show a significant parameter capable of interfering with the results when changing the spacing between the tendons. It was identified that the *fib* model code [14] presents the best estimates even in the LoA III approximation, where the code considers that this level is not suitable for estimating cracked elements. ACI [11] was the most conservative in the estimates.
2. Series T: it was observed that the *fib* model code [14] has the best trend of results as the thickness of the slab is increased; additionally, there is little difference in the results in its two levels of approximation. In general, the other standards tend to show the same behavior, except for ACI [11], which is characterized by more conservative behavior in estimates.

3. Series C: the predictions of Eurocode 2 [12] and NBR [13] follow the same trend of behavior, differing due to the scale factor k . Considering the coefficient of variation and the average, the best results were due to NBR [13], followed by ACI [11]. In the case of the ACI [11], better predictions were noted with the increase in the rectangularity of the column. For the *fib* model code [14], it is observed that, in levels II and III, there is a stability of the results from the C-40 Series, which is justified due to the discontinuity of the critical perimeter, limited to $3d$.

With the analyses presented for the numerical and theoretical models, it was possible to identify the influence that the spacing between the prestressing tendons, the thickness of the slab, and the rectangularity of the column exert on punching resistance. When comparing the two analyses, it was noted that the loads predicted by the numerical models were greater than those estimated by the standards. In general, the two analyses together can help to improve some limitations identified by the design codes, and help designers decide which parameter can be changed in the search for the best possible efficiency for the punching resistance of prestressed flat slabs.

Many parameters that have a significant influence on the resistance capacity of these structures need to be clarified. Thus, some guidelines for the development of future investigations are:

- It is proposed to use the constitutive model adopted in this work to simulate more experimental tests of slabs and beams, as well as other types of reinforced and prestressed concrete structures, such as columns, corbels, and shells.
- The simulation of isolated connections between columns and slabs is adequate for the localized punching analysis, but it does not cover the existing membrane forces in the global model (panels of slabs). With the facilities offered by computational tools, it would be interesting to model a slab supported by several pillars to study this phenomenon.
- Regarding prestressing, little information was found in the literature review and in the standards regarding the differences between the types of prestressing (bonded or unbonded). It is recommended to carry out a study to compare these two alternatives in behavior from flat slabs to punching. An experimental study of prestressed slabs is also suggested to confirm the numerical results achieved in this research.
- It is proposed to perform modeling of concrete slabs with shear reinforcement, varying the number of layers and radial spacing between elements.
- It is proposed to analyze punching situations for slabs with applied moments (eccentric punching).

Author Contributions: H.B.: Conceptualization, Formal analysis, Investigation, Methodology, Validation, Writing—original draft, Writing—review and editing. L.J.A.: Visualization, Writing—review and editing. M.G.M.: Formal analysis, Methodology, Visualization, Writing—review and editing. E.A.P.L.: Supervision, Writing—review and editing. All authors have read and agreed to the published version of the manuscript.

Funding: This research received no external funding.

Data Availability Statement: Data available on request from the authors.

Acknowledgments: This research was financed in part by the Coordenação de Aperfeiçoamento de Pessoal de Nível Superior-Brasil (CAPES)-Finance Code 001.

Conflicts of Interest: The authors declare no conflict of interest.

Appendix A

For flat slabs without shear reinforcement, the critical perimeters are drawn according to Figure A1.

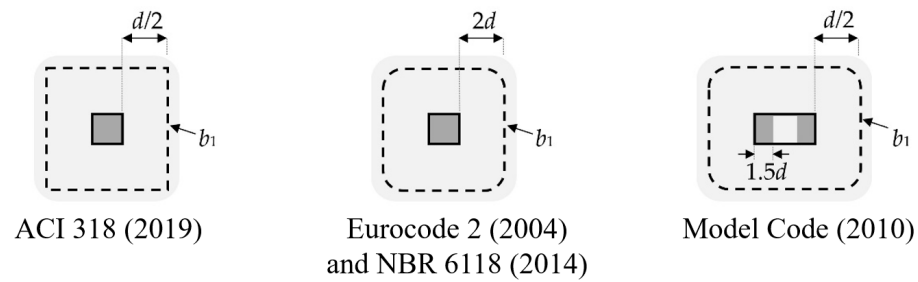


Figure A1. Perimeters for punching verification according to current codes [11–14].

To facilitate understanding, the expressions of the standards are changed to represent the ultimate load (V_R), differentiating by the subindexes with the abbreviations of each normative code, and the other parameters, with the same uniform nomenclature according to the following equations for dimensioning prestressed flat slabs.

ACI [11]:

$$V_{R,ACI} = \min. \left\{ \begin{array}{l} \left[\frac{3.5}{12} \lambda \sqrt{f_c} + 0.3 \sigma_{cp} + \frac{V_p}{b_1 d} \right] b_1 d \\ \left[\frac{1}{12} \left(1.5 + \frac{\alpha_s d}{b_1} \right) \lambda \sqrt{f_c} + 0.3 \sigma_{cp} + \frac{V_p}{b_1 d} \right] b_1 d \end{array} \right. \quad (A1)$$

Eurocode 2 [12]:

$$V_{R,EC} = \left[\frac{0.18}{\gamma_c} (1 + k) (100 \rho f_c)^{1/3} + 0.10 \sigma_{cp} \right] b_1 d + V_p \quad (A2)$$

NBR [13]:

$$V_{R,NBR} = \left[0.18 (1 + k) (100 \rho f_c)^{1/3} + 0.10 \sigma_{cp} \right] b_1 d + V_p \quad (A3)$$

fib Model Code [14]:

$$V_{R,MC} = k_\psi \frac{\sqrt{f_c}}{\gamma_c} b_1 d + V_p \quad (A4)$$

where:

$$k_\psi = \frac{1}{1.5 + 0.9 \psi d k_{dg}} \leq 0.6 \quad (A5)$$

$$k_{dg} = \frac{32}{16 + d_g} \geq 0.75 \quad (A6)$$

Furthermore, d_g is the maximum aggregate size in mm and ψ is the slab rotation. In the case of prestressed slabs, rotation can be calculated using Equations (A7) and (A8).

$$\psi = 1.5 \frac{r_s}{d} \frac{f_{ys}}{E_s} \left(\frac{m_{sd} - m_p}{m_{Rd} - m_p} \right)^{1.5} \quad \text{LoAII} \quad (A7)$$

$$\psi = 1.2 \frac{r_s}{d} \frac{f_{ys}}{E_s} \left(\frac{m_{sd} - m_p}{m_{Rd} - m_p} \right)^{1.5} \quad \text{LoAIII} \quad (A8)$$

where r_s is the distance between the geometric center of the column and the radius at which the bending moment is zero; f_{ys} is the design value of the bending reinforcement yield stress; E_s : modulus of elasticity of bending reinforcement; m_{sd} is the average bending moment per unit width in the control strip; $b_s = 1.5 r_s$, or internal slab–column connections, where it can be considered $V_{Ed}/8$ (V_{Ed} is the shear force acting on the slab); m_{Rd} : average design flexural strength per unit length in a loaded range, according to Equation (A9).

$$m_{Rd} = \rho f_{ys} d^2 \left(1 - \frac{\rho f_{ys}}{2 f_c} \right) \quad (A9)$$

where m_p is the moment of decompression in the width of the band b_s , which can be determined by the isostatic moment of the prestressing according to the equation:

$$m_p = \frac{N_p e_p}{b_s} \quad (\text{A10})$$

N_p is the normal force due to the sum of the prestressing of each strand that intersects the control strip (b_s); e_p is the eccentricity of the normal force in relation to the geometric center of the section at the point where the prestressing tendons intersect the control perimeter (b_1).

The equation for the average bending-resistant moment per unit length of the slab is also modified to consider the effect of compression generated by prestressing.

$$m_{Rd} = \rho d f_y \left(d - \frac{h}{2} \right) + f_{cp} \chi_{pl} \left(\frac{h}{2} - \frac{\chi_{pl}}{2} \right) \quad (\text{A11})$$

where f_{cp} : plastic strength of concrete, given by $f_{cp} \left(\frac{30 \text{ MPa}}{f_c} \right)^{\frac{1}{3}} \leq f_c$ and χ_{pl} : height of the concrete's compressed region in the section, assuming a constant plastic stress distribution.

$$\chi_{pl} = \frac{(\rho d f_y - \sigma_p h)}{f_{cp}} \quad (\text{A12})$$

The other indices are:

b_1 : critical control perimeter, according to each standard;

d : effective depth;

f_c is the compressive strength of concrete;

k : scale factor, $\sqrt{200/d}$, in (mm). For Eurocode 2 [12] consider $k \leq 2.0$;

V_p : increase in vertical force due to prestressing in the b_s control range for the *fib* model code [14]. For ACI [11], EC2 [12], and NBR [13], it is calculated in the critical control perimeter b_1 .

α_s : constant, equal to 40 for internal columns;

λ : concrete modification factor equals to 1.0 for normal weight concrete between 21.55 and 25.60 kN/m³;

σ_{cp} : average compressive stress caused by prestressing;

γ_c : the value of 1.0 was assigned to determine the maximum value of the resistant load;

ρ : flexural reinforcement ratio. The average of the reinforcement rate in the bars of the x and y directions was considered.

References

- Melges, J.L.P. Experimental Punching Shear Analysis of Reinforced and Prestressed Concrete Slabs. Ph.D. Thesis, São Carlos School of Engineering, University of São Paulo, São Carlos, Brazil, 2001. Available online: <http://www.teses.usp.br/teses/disponiveis/18/18134/tde-07062006-152744/> (accessed on 27 March 2023).
- Vecchio, F.J.; Gauvreau, P.; Liu, K. Modeling of unbonded post-tensioned concrete beams Critical in Shear. *ACI Struct. J.* **2006**, *103*, 57–64.
- El-Sisi, A.A.; Hassanin, A.I.; Shabaan, H.F.; Elsheikh, A.I. Effect of external post-tensioning on steel–concrete composite beams with partial connection. *Eng. Struct.* **2021**, *247*, 1–15. [CrossRef]
- Grow, J.; Vanderbilt, M. Shear strength of prestressed lightweight aggregate concrete flat plates. *Precast./Prestress. Concr. Inst J.* **1967**, *5*, 18–28. [CrossRef]
- Nylander, H.; Kinnunen, S.; Ingvarsson, H. *Punching of A Prestressed and Normally Reinforced Concrete Bridge Slab Supported by A Column*; Technical Report; KTH Royal Institute of Technology: Stockholm, Sweden, 1977.
- Pralong, J.; Brändli, W.; Thürlimann, B. *Durchstanzversuche an Stahlbetonund Spannbetonplatten*. 7305; Birkhäuser: Basel, Switzerland, 1979.
- Shehata, I. Punching of Prestressed and Non-Prestressed Reinforced Concrete Flat Slabs. Ph.D. Thesis, Polytechnic of Central London, London, UK, 1982.
- Corrêa, G. Puncionamento em Lajes Cogumelo Protendidas com Cabos não Aderentes. Master' Thesis, University of Brasilia, Brasília, Brazil, 2001. Available online: <https://repositorio.unb.br/handle/10482/37391> (accessed on 27 March 2023).
- Ramos, A.P.; Lúcio, V.J.; Regan, P.E. Punching of flat slabs with in-plane forces. *Eng Struct.* **2011**, *33*, 894–902. [CrossRef]

10. Clément, T.; Ramos, A.P.; Ruiz, M.F.; Muttoni, A. Influence of prestressing on the punching strength of post-tensioned slabs. *Eng. Struct.* **2014**, *72*, 56–69. [\[CrossRef\]](#)
11. ACI 318-19; Building Code Requirements for Structural Concrete and Commentary. American Concrete Institute: Farmington Hills, MI, USA, 2019.
12. EN 1992-1-1; Eurocode 2, Design of Concrete Structures—Part 1-1: General Rules and Rules for Buildings. CEN: Belgium, Belgium, 2010.
13. ABNT NBR 6118; Design of Concrete Structures—Procedures. Brazilian Association of Technical Standards: Rio de Janeiro, Brazil, 2014.
14. fib (Fédération Internationale du Béton). *fib Model Code for Concrete Structures 2010 (MC 2010)*; Ernst and Sohn: Berlin, Germany, 2013.
15. Ellobody, E.; Bailey, C.G. Behaviour of Unbonded post-tensioned one-way concrete slabs. *Adv. Struct. Eng.* **2008**, *11*, 107–120. [\[CrossRef\]](#)
16. Kang, T.H.K.; Huang, Y.; Shin, M.; Lee, J.D.; Cho, A.S. Experimental and numerical assessment of bonded and unbonded post-tensioned concrete members. *ACI Struct. J.* **2015**, *112*, 735–748. [\[CrossRef\]](#)
17. Diaz, R.A.; Trautwein, L.M.; Bittencourt, T.N. Numerical investigation of the punching shear capacity of unbonded post-tensioned concrete flat slabs. *Struct. Concr.* **2020**, *22*, 1205–1222. [\[CrossRef\]](#)
18. Červenka, V.; Jendele, L.; Červenka, J. *ATENA Program Documentation Part 1 Theory*; Červenka Consulting s.r.o.: Prague, Czech Republic, 2016; p. 282.
19. Bažant, Z.P.; Oh, B.H. Crack band theory for fracture of concrete. *Mat. Constr.* **1983**, *16*, 155–177. [\[CrossRef\]](#)
20. Menetrey, P.; Willam, K.J. Triaxial failure criterion for concrete and its generalization. *Struct. J.* **1995**, *92*, 311–318.
21. Červenka, J.; Papanikolaou, V.K. Three-dimensional combined fracture–plastic material model for concrete. *Int. J. Plast.* **2008**, *24*, 2192–2220. [\[CrossRef\]](#)
22. De Borst, R.; Crisfield, M.A.; Remmers, J.J.; Verhoosel, C.V. Solution Techniques in Quasi-static Analysis. In *Nonlinear Finite Element Analysis of Solids and Structures*; John Wiley & Sons: Hoboken NJ, USA, 2012; pp. 113–116. [\[CrossRef\]](#)
23. Vecchio, F.J.; Collins, M.P. Modified Compression-Field Theory for reinforced concrete beams subjected to shear. *ACI J. Proc.* **1986**, *83*, 219–231.
24. Comité Euro-International du Béton. *CEB-FIP Model Code 1990*; Thomas Telford: London, UK, 1993.
25. Hordijk, D.A. Local Approach to Fatigue of Concrete. Ph.D. Thesis, Delft University of Technology, Delft, The Netherlands, 1991.
26. Vos, E. Influence of Loading Rate and Radial Pressure on Bond in Reinforced Concrete. Dissertation, Delft University, Delft, The Netherlands. 1983, pp. 219–220. Available online: <https://repository.tudelft.nl/islandora/object/uuid:29419e9e-9b56-41a5-94cb-d363b1c8c15e> (accessed on 27 March 2023).
27. Kupfer, H.; Hilsdorf, H.K.; Rüsch, H. Behavior of concrete under Biaxial Stress. *J. ACI* **1969**, *66*, 656–666.
28. Bigaj, A.J. Structural Dependence of Rotations Capacity of Plastic Hinges in R.C. Beams and Slabs. Doctoral Thesis, Delft University of Technology, Delft, The Netherlands, 1999. Available online: <http://resolver.tudelft.nl/uuid:f7b89645-75f5-463a-bec5-7da4afeb537b> (accessed on 27 March 2023).

Disclaimer/Publisher’s Note: The statements, opinions and data contained in all publications are solely those of the individual author(s) and contributor(s) and not of MDPI and/or the editor(s). MDPI and/or the editor(s) disclaim responsibility for any injury to people or property resulting from any ideas, methods, instructions or products referred to in the content.